Influence of the Subcloud Layer on the Development of a Deep Convective Ensemble

STEVEN J. BÖING AND HARM J. J. JONKER

Delft University of Technology, Delft, Netherlands

A. PIER SIEBESMA

Delft University of Technology, Delft, and Royal Netherlands Meteorological Institute (KNMI), De Bilt, Netherlands

WOJCIECH W. GRABOWSKI

National Center for Atmospheric Research, Boulder, Colorado

(Manuscript received 15 November 2011, in final form 11 March 2012)

ABSTRACT

The rapid transition from shallow to deep convection is investigated using large-eddy simulations. The role of cold pools, which occur due to the evaporation of rainfall, is explored using a series of experiments in which their formation is suppressed. A positive feedback occurs: the presence of cold pools promotes deeper, wider, and more buoyant clouds with higher precipitation rates, which in turn lead to stronger cold pools. To assess the influence of the subcloud layer on the development of deep convection, the coupling between the cloud layer and the subcloud layer is explored using Lagrangian particle trajectories. As shown in previous studies, particles that enter clouds have properties that deviate significantly from the mean state. However, the differences between particles that enter shallow and deep clouds are remarkably small in the subcloud layer, and become larger in the cloud layer, indicating different entrainment rates. The particles that enter the deepest clouds also correspond to the widest cloud bases, which points to the importance of convective organization within the subcloud layer.

1. Introduction

a. Deep convection and the diurnal cycle

The diurnal cycle of cloud development over land in the tropics is characterized by a rapid development of large cumulonimbus clouds in the afternoon. During the morning, deep convection fails to develop, despite the occurrence of large values of convective available potential energy (CAPE). As the intensity of parameterized deep convection in many numerical weather prediction (NWP) and climate models is largely determined by the availability of CAPE, deep convection develops too early in these models, leading to a systematic bias in a too-early onset of precipitation in the diurnal cycle (Betts and Jakob 2002; Guichard et al. 2004; Bechtold et al. 2006).

Large-eddy simulation (LES) can be used to study the diurnal cycle of deep convection in the absence of strong synoptic forcing. Such conditions have been found, for example, during the Tropical Rainfall Measuring Mission Large-Scale Biosphere–Atmosphere (TRMM-LBA) measurement campaign in Brazil (Silva Dias et al. 2002). Grabowski et al. (2006) based a model intercomparison study case on observations from this campaign. This case has been run in high-resolution LES by Khairoutdinov and Randall (2006) and Lang et al. (2007). Wu et al. (2009) used an idealized version of this case to look into the role of tropospheric temperature and moisture profiles in the diurnal cycle in a two-dimensional cloud-resolving model. In these idealized simulations, deep convection developed gradually over the course of several hours despite the availability of large values of CAPE. A suppressing factor on the development of deep convection is the occurrence of a convective inhibition (CIN) layer, where the buoyancy of rising parcels becomes negative. However, Wu et al. (2009) found the convective inhibition to be smallest early in the simulation, when shallow clouds start to form, rather than during the deep phase.

Corresponding author address: Steef Böing, TU Delft, P.O. Box 5046, 2600 GA Delft, Netherlands.
E-mail: s.j.boing@tudelft.nl

DOI: 10.1175/JAS-D-11-0317.1

b. Role of the subcloud layer

Once precipitation occurs, liquid water loading and the evaporation of rain cause the formation of negatively buoyant downdrafts. If these downdrafts reach the bottom of the subcloud layer, they spread over the surface in the form of a density current that laterally propagates away from the rainfall. These density currents often appear in circular patterns, which are known as cold pools. Although the outflow boundaries of the cold pools are often associated with high relative humidity, downdrafts cause the inflow of cold and dry air at the centers of the cold pools.

After an initial shallow phase, the transition from shallow to deep convection becomes more rapid (e.g., in terms of cloud-top height) around the time when precipitation starts. Khairoutdinov and Randall (2006) found that in a high-resolution three-dimensional simulation, the rapid growth of deep convection could be prevented when the evaporation of rainfall was suppressed in the microphysics scheme. Wu et al. (2009), however, argue that a rapid transition in cloud height precedes the formation of cold pools and that rather than the occurrence of cold pools, mean cloud buoyancy is crucial for the onset of deep convection. Martins (2011) found that the growth of length scales in the subcloud layer is strongly correlated with the presence of precipitation. Zhang and Klein (2010), on the other hand, argue on the basis of observations that the moisture and moist static energy inhomogeneity in the boundary layer is a good indicator of the transition to deep convection. In their analysis, the increase of boundary layer inhomogeneity precedes the formation of precipitation.

Two mechanisms by which cold pools can accelerate the transition from shallow to deep convection have been proposed. Dynamical effects play a key role in the first mechanism. Forced uplift at the outflow boundary (the edge of a cold pool), where a gust front occurs, can act as a catalyst for deep convection (Krueger 1988; Khairoutdinov and Randall 2006). Initiation of new convection at the gust front has been observed both in precipitating shallow convection over the ocean (e.g., Rauber et al. 2007; Zuidema et al. 2012), midlatitude continental deep convection (e.g., Weckwerth and Wakimoto 1992), and tropical deep convection during TRMM-LBA (Lima and Wilson 2008). The Lima and Wilson study found that preferential convective triggering at the interface of colliding outflow boundaries occurred in the afternoon. Outflow boundaries can also interact with a sea-breeze circulation to trigger convection, as was found in studies of convective initiation over Florida and the Tiwi islands (Kingsmill 1995; Wilson and Megenhardt 1997; Carbone et al. 2000). Rio et al. (2009) show how a parameterization of the dynamic effects of the wake can contribute to a more realistic timing of parameterized deep convection.

In the second mechanism, enhanced updraft activity occurs because of a change in the thermodynamic properties of the subcloud layer. Although parcels in the middle of the cold pool tend to be relatively dry and too cold to act as a source of buoyant updrafts, relatively warm and moist air may develop at the edge of the outflow boundary, for example due to the action of surface fluxes or simply in contrast to the mean state. Tompkins (2001a) argues that for deep convection over the ocean, thermodynamic rather than dynamic forcing plays an important role.

c. Other factors influencing deep convection

Besides the presence of cold pools, several other factors are known to play a role in enhancing the strength of deep convection. First, the relative humidity of the middle troposphere is crucial for the onset of congestus clouds. A dry atmosphere suppresses the growth of deep clouds, and moistening (e.g., by shallow clouds or a reduction of large-scale drying) is necessary to overcome this inhibition. This was confirmed in simulations (Derbyshire et al. 2006; Wu et al. 2009; Waite and Khouider 2010) and in an observational study (Holloway and Neelin 2009). Large-scale upward motion helps to premoisten the atmosphere and enhance convective activity (Krueger 1988; Xie et al. 2010).

In addition, wind shear may organize the convection into squall lines (Rotunno et al. 1988; Robe and Emanuel 2001; Parker 1996). Particularly if the cold pool moves at the same speed as the convection above, the development of deep clouds may be enhanced (Moncrieff and Liu 1999).

d. Purpose of the current work

In this study, we will focus on the role of the dynamics and thermodynamics in the subcloud layer, and confine ourselves to a case with a prescribed initial relative humidity profile and without wind shear. We use the Dutch Atmospheric Large-Eddy Simulation (DALES) model to systematically investigate the mechanisms by which evaporation in the subcloud layer affects the transition from shallow to deep convection. We investigate the role of the positive feedback loop sketched in Fig. 1 in accelerating this transition. Evaporation in the subcloud layer leads to the formation of cold pools. Because of changes in the thermodynamic and/or dynamic properties of the subcloud layer, wider clouds with lower entrainment rates (Grabowski et al. 2006) and larger

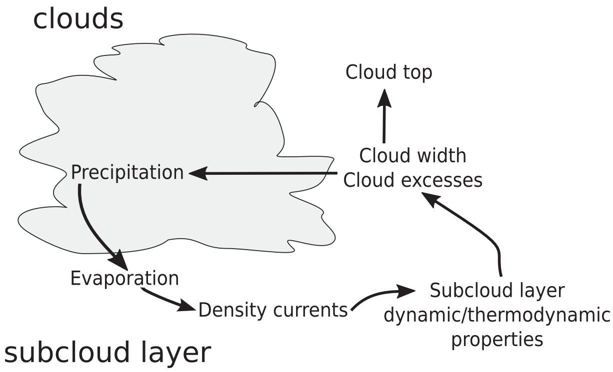

FIG. 1. The feedback loop between rainfall and the subcloud layer investigated in this paper.

excesses of thermodynamic variables (i.e., higher specific humidity and moist static energy) appear at the outflow boundaries, as suggested by Khairoutdinov and Randall (2006). These clouds reach higher into the troposphere, and a larger fraction of their moisture excess is converted into precipitation, which completes the feedback loop.

Figure 2 shows another reason to investigate this feedback loop in more detail. In the simulation we reduced the variances of the thermodynamic variables by using a (variable) damping time scale τ. The implementation details are given in section 2c, but briefly, the smaller τ is, the stronger the damping of the variance. The damping was applied only to the subcloud layer. As Fig. 2 shows, the mean rainfall decreases dramatically as a result of the variance reduction. As such it draws attention to the subcloud layer and provides a way to disentangle the feedback loop and learn more about the underlying mechanism by which subcloud layer (thermo)dynamics influences the cloud layer.

This paper is organized as follows. In section 2, we will describe the case setup and the methodology we use to modify certain aspects of the simulation. In section 3, we explore how these changes affect the overall properties of the subcloud layer and the conditionally sampled cloud core. Section 4 contains the Lagrangian particle study, which focuses on the mechanism by which wider clouds form. We will consider both the dynamic and thermodynamic effects in the subcloud layer (although these effects are tightly coupled; e.g., the negative buoyancy of downdrafts largely determines the speed at which the cold pool propagates). Making use of Lagrangian particle trajectories enables us to study the differences between deeper and shallower clouds, and allows us to investigate the coupling between the subcloud layer and the cloud layer in an intuitive framework. We will relate our findings to earlier studies in section 5.

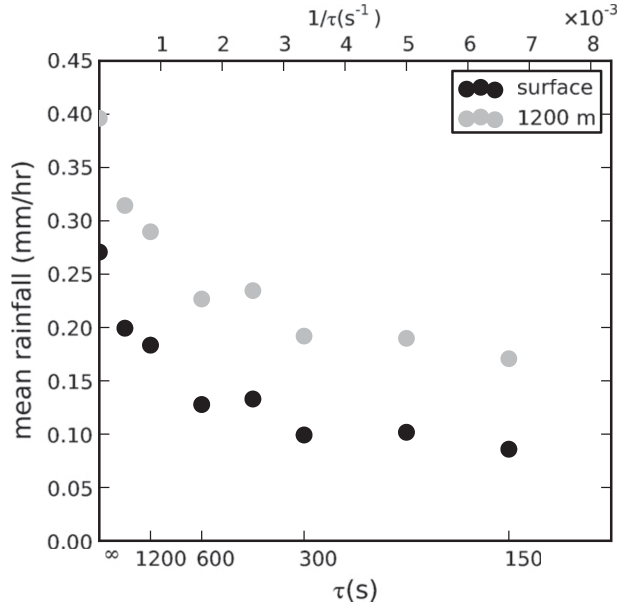

FIG. 2. Domain mean rainfall rate as a function of the time scale τ used for damping the variance in the subcloud layer. The top axis shows $1/\tau$. The mean rainfall rates during the eighth hour of the simulation at the surface and at 1200 m, above the subcloud layer, are plotted. Section 2 mentions the simulation setup.

2. Method and case

a. Large-eddy simulation model

The DALES model is described in Heus et al. (2010). It uses a prognostic subfilter-scale turbulent kinetic energy equation to calculate subgrid-scale transports. To run deep convective cases, the anelastic approximation was implemented for the momentum and scalar transport equations. The anelastic approximation follows Smolarkiewicz et al. (2001) and is extended to the subgrid stress scheme. The prognostic variables are total nonprecipitating water specific humidity ($q_t = q_v + q_c$, where q_v denotes water vapor and $q_c = q_l + q_i$ the sum of cloud liquid water and cloud ice), total hydrometeor specific humidity q_r and linear liquid water potential temperature [$\theta_l = \theta - L_v q_c/(c_p\Pi)$]. This formulation of θ_l is an approximation to more elaborate versions (e.g., Bryan and Fritsch 2004; Romps and Kuang 2010b), and quantitative errors may arise at large values of q_c, such as occur in moist adiabats. In the current study, however, q_c is limited by mixing and fallout. The θ_l sources due to precipitation are modeled such that temperature is preserved in the transition from q_c to q_r, as if this transition were reversible:

$$\frac{\partial}{\partial t}\theta_l\bigg|_{\text{microphysics}} = -\frac{L_v}{c_p\Pi}\frac{\partial}{\partial t}q_c\bigg|_{\text{microphysics}}. \qquad (1)$$

As in Grabowski (1998), we ignore the latent heat of freezing. Taking into account the latent heat of freezing provides an extra source of kinetic energy for rising updrafts and would thus allow for deeper convection, but it would also create a stronger discontinuity in the development of the convection. The melting layer dynamics are also not taken into account. Melting of precipitation would generate additional downdrafts around the 5-km level. A single-moment ice microphysics scheme, based on the work of Grabowski (1998) and Tomita (2008), is used to predict specific humidities corresponding to snow, rain, and graupel. Modifications to the scheme and its implementation in DALES are summarized in the appendix.

b. Case and LES setup

We use an idealized version of the intercomparison case of Grabowski et al. (2006), which is documented in Wu et al. (2009; their M85 case). No large-scale vertical wind shear is present and surface sensible and latent heat fluxes are held constant at 161 and 343 W m^{-2}, respectively. These fluxes are representative of the average fluxes during the morning transition in the TRMM-LBA case and are much stronger than typical fluxes over the ocean. We chose to prescribe the fluxes in accordance with the case setup, rather than use a more detailed interactive land surface scheme. This means the larger surface fluxes that are triggered at the gust front in an interactive scheme are not taken into account. Although the influence of the land surface and its properties would merit further investigation, our approach allows us to focus on the internal dynamics of the cold pools. The initial profiles of potential temperature lapse rate and relative humidity in this simulation are shown in Fig. 3. In contrast to Wu et al. we run the simulation in a three-dimensional model. To accommodate convection reaching up to the tropopause, we extend the temperature profile using a linearly increasing lapse rate above 14.5 km (with a slope that matches the intercomparison case setup). The advantage of the M85 setup is that it allows us to focus on the intrinsic characteristics of the transition. A drawback is that both the absence of wind shear and the absence of strong fluxes at the end of the simulation contribute to a slower development of precipitation. To obtain convection with a considerable precipitation rate, the M85 simulation was extended from 6 to 8 h. We have repeated the simulations in section 3 for the original (Grabowski et al. 2006) case and found similar results, although mesoscale organization due to vertical wind shear played a larger role for that case.

Doubly periodic boundary conditions were used, with a domain size of 57 600 m in both horizontal directions and a grid spacing of 150 m. Previous work (Bryan et al. 2003; Lang et al. 2007; Martins 2011) has shown that a grid spacing of less than 250 m is needed in order to obtain the correct timing of the transition from shallow to deep convection. We repeated the reference experiment with half the horizontal grid spacing, and once more using twice the domain size. Differences were small, although the experiments with half the grid spacing had a somewhat delayed transition to deep convection. In the vertical, a stretched grid of 256 points was used with a spacing exponentially increasing from 40 m at the surface to 195 m at the domain top.

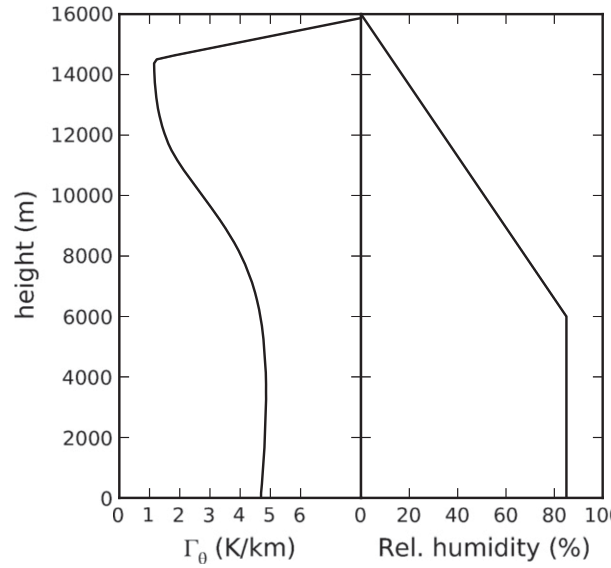

FIG. 3. Initial profiles of (left) potential temperature lapse rate and (right) relative humidity for the M85 case.

The LES was initialized with random θ_l perturbations with a uniform distribution between ± 0.1 K. The absence of initial large-scale structures may somewhat delay the development of deep convection (Stirling and Petch 2004).

c. Subcloud layer modifications in LES

The feedback loop is investigated using several experiments in which we modify particular aspects of the subcloud layer. In all simulations, the top of the subcloud layer is identified by the local minimum of the buoyancy flux that occurs at this level. The following experiments were conducted:

(i) A reference case in which no modifications to the subcloud layer are made.
(ii) Evaporation of rain is removed altogether [as in Khairoutdinov and Randall (2006)]. This modification takes place both in the subcloud layer and above cloud base, hence both the formation of downdrafts in the cloud layer and cold pools in the subcloud layer are affected. All of the precipitation

that forms in these simulations will reach the surface, where it is removed from the simulation.

(iii) The moisture and temperature tendencies due to evaporation are horizontally homogenized in the subcloud layer. The microphysics scheme is run each time step to determine the tendencies due to evaporation. Yet instead of applying the local tendency, we apply the horizontally averaged tendency to the fields of θ_l and q_t. This intervention does not take place in the cloud layer, and some of the precipitation is evaporated at higher levels. Nevertheless, this modification is enough to suppress most of the cold pool formation. Although a negative feedback on evaporation that occurs in the reference simulation due to the saturation of air below cloud base is suppressed using this modification, the impact of this modification on the mean properties of the subcloud layer is smaller than when evaporation is ignored altogether.

(iv) Evaporation is left intact, but fluctuations of the θ_l and q_t field in the subcloud layer are damped with a time scale τ:

$$\frac{\partial}{\partial t}\theta_l = \cdots - \frac{1}{\tau}(\theta_l - \overline{\theta_l}) \quad \text{if} \quad z < z_{\text{cb}}, \qquad (2)$$

$$\frac{\partial}{\partial t}q_t = \cdots - \frac{1}{\tau}(q_t - \overline{q_t}) \quad \text{if} \quad z < z_{\text{cb}}. \qquad (3)$$

This operation conserves the mean values of the thermodynamic properties in the subcloud layer, but diminishes the variance. By varying τ, we can control the strength of the variance damping. In the current work we focus on results with $\tau = 600$ s. As we can see in Fig. 2, at $\tau = 600$ s the domain mean precipitation is largely suppressed. However, convection will still be able to generate turbulence in the boundary layer (which acts on similar time scales as the damping). The experiments with $\tau = 150$ s strongly suppress all fluctuations in the prognostic variables, also those generated by convection in the boundary layer.

3. Effects of subcloud layer modifications

a. The transition in the reference and modified runs

Figure 4 shows the development of the maximum cloud-top height and precipitation rate in the reference case. Wu et al. (2009) found that after 3–5 h the cloud center of mass started rising faster than linearly in their simulations, and they used this to identify the timing of the transition from shallow to deep convection. Unlike Wu et al. we find the cloud center of mass to rise linearly until well after the onset of precipitation. This may be due to the slower premoistening in three-dimensional simulations as compared with two-dimensional ones (e.g., Petch et al. 2008), as well as to differences in microphysics schemes. Grabowski et al. (2006) show that there is a wide spread in the development of cloud center of mass in the TRMM-LBA intercomparison case. A rapid transition in maximum cloud-top height, as identified by a cloud condensate threshold, takes place after the onset of precipitation (although only small amounts of precipitation are present when the transition starts). For the different simulations, the cloud condensate and hydrometeor specific humidity averaged over the fifth (240–300 min) and eighth hours (420–480 min) of the simulation are shown in Fig. 5. Whereas the differences in cloud condensate are small after 240–300 min, after 420–480 min the profiles have diverged significantly with anvils forming in the reference case, but not in the other cases. We will show later that these anvils mainly correspond to the largest clouds in the ensemble. The differences around cloud base are smaller, with the modified cases even showing slightly higher cloud condensate content at cloud base. The difference in hydrometeor content is up to a factor of 2 and visible throughout the cloud layer. The experiments where homogenization of evaporation takes place, or damping is applied to the thermodynamic variables, show a decrease in q_r in and slightly above the subcloud layer with a slope similar to the original case. This is related to the strength of evaporation, and hence the development of the mean properties in the subcloud layer, which is discussed below.

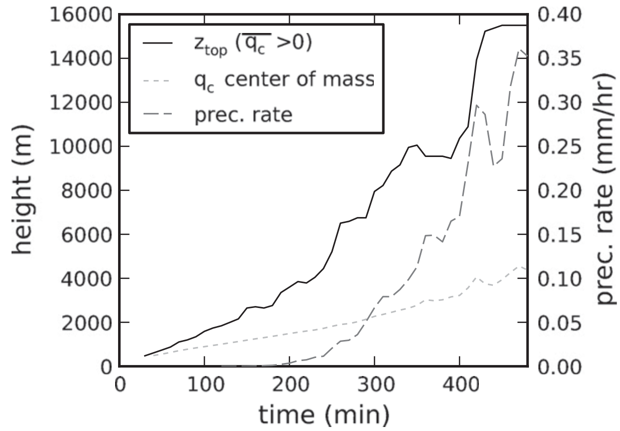

FIG. 4. Maximum cloud-top height and precipitation rate during the transition from shallow to deep convection for the reference case.

The mean virtual potential profile is slightly affected (Fig. 6) in the damping and homogenized evaporation experiments, but much less than when ignoring evaporation altogether. Because the mean state is closer to that of the reference simulation, we will focus on the damping and homogenized evaporation experiments in this

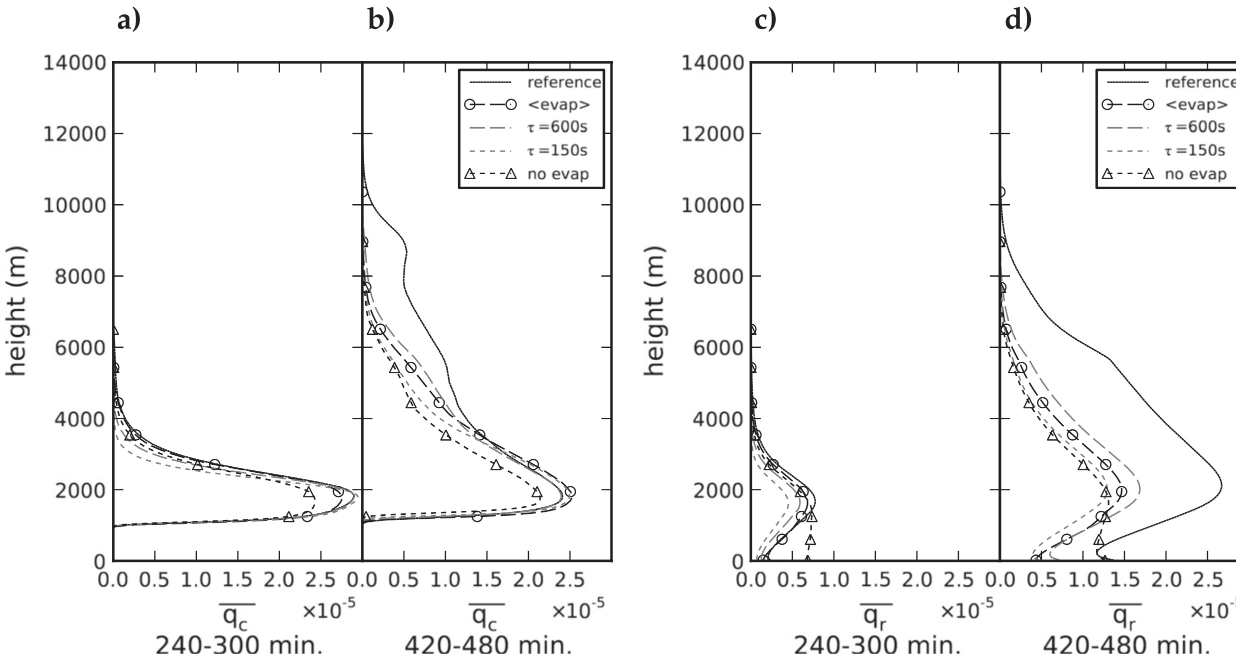

FIG. 5. (a),(b) Cloud condensate and (c),(d) total precipitation specific humidities, mean value of the (a),(c) fifth and (b),(d) eighth simulation hours. "No evap" indicates evaporation of rain fully left out and "⟨evap⟩" indicates evaporation homogenized over horizontal plane; τ is the damping time scale for thermodynamic fluctuations in the subcloud layer.

paper. In the reference case, there is a cold pool signature in the lower boundary layer that appears as a weak mean stratification which does not appear in the other cases. The moisture content in the subcloud layer also deviates from the reference simulation for the experiment without evaporation, showing that the net effect of evaporation is a moistening of the boundary layer in the present case (Fig. 6). Above the boundary profile, we found the reference simulation to have deeper clouds but lower average specific humidity in most of the cloud layer as compared with the modified cases (this is shown for the lower cloud layer in Fig. 6 but also holds for higher levels). The latter is a consequence of the fact that the surface fluxes are the same for each simulation, but the loss of moisture due to rainfall is highest in the reference case.

Surface rainfall tends to occur only under the widest clouds, in columns where the cloud condensate (nonprecipitating liquid water and ice) path is high, as can be seen in Fig. 7. This figure shows surface rainfall rate and cloud condensate path after 420 min in the reference

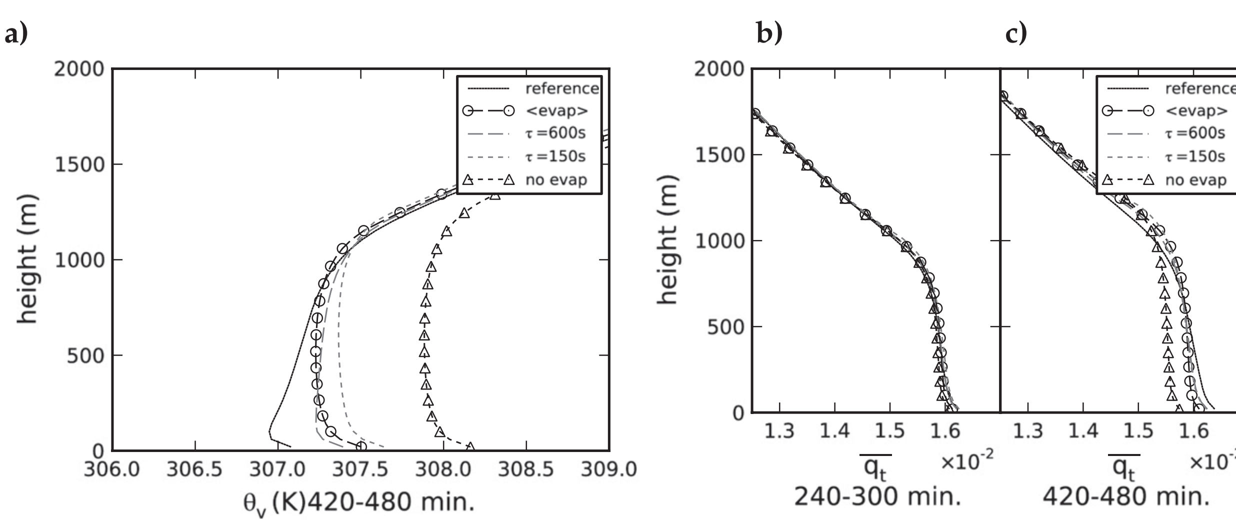

FIG. 6. (a) Boundary layer mean θ_v profile in the eighth hour, and boundary layer mean q_t profile in the (b) fifth and (c) eighth hours.

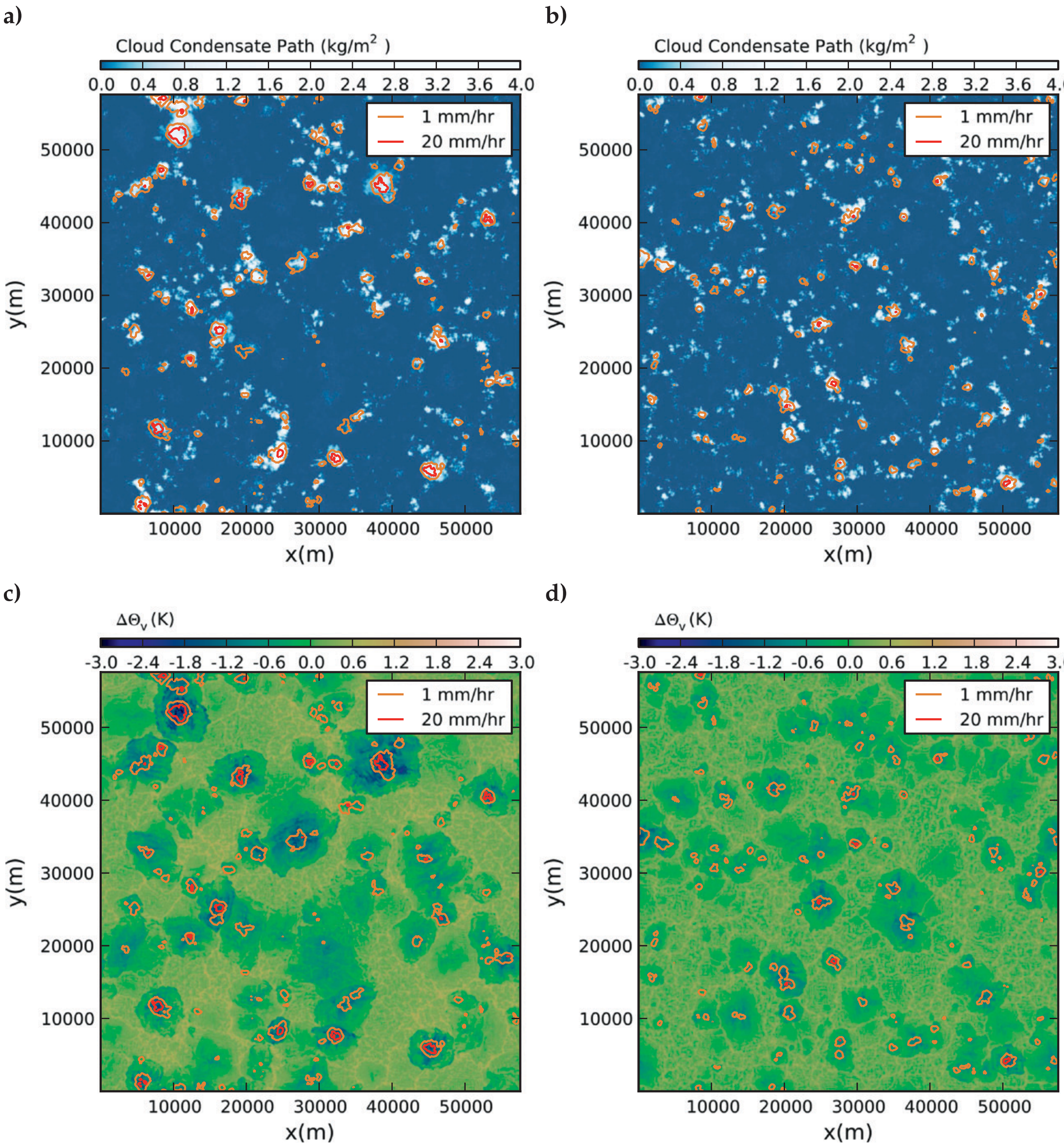

FIG. 7. (a),(b) Cloud condensate path and (c),(d) 100-m buoyancy in (a),(c) the reference simulation and (b),(d) a modified simulation in which the subcloud variance of the thermodynamic variables (q_t and θ_l) was damped with $\tau = 600$ s. Contours indicate surface precipitation rate. Cross sections 420 min after the start of the simulation.

simulation and a simulation with $\tau = 600$ s. The corresponding subcloud layer buoyancy structures at 100 m are also shown. Cold pool size has decreased dramatically as a result of damping the variance of moisture and temperature in the subcloud layer, and the magnitude of both the positive and negative virtual potential temperature extremes has diminished. Damping has apparently also resulted in the disappearance of large-scale structures in the cloud layer, as seen in Figs. 7a,b. Cross sections for the case where evaporation is homogenized or fully left out are not shown here, but these also indicate the absence of the widest clouds, with an even stronger reduction in length scales because the cold pool formation is fully suppressed in these simulations. We also show

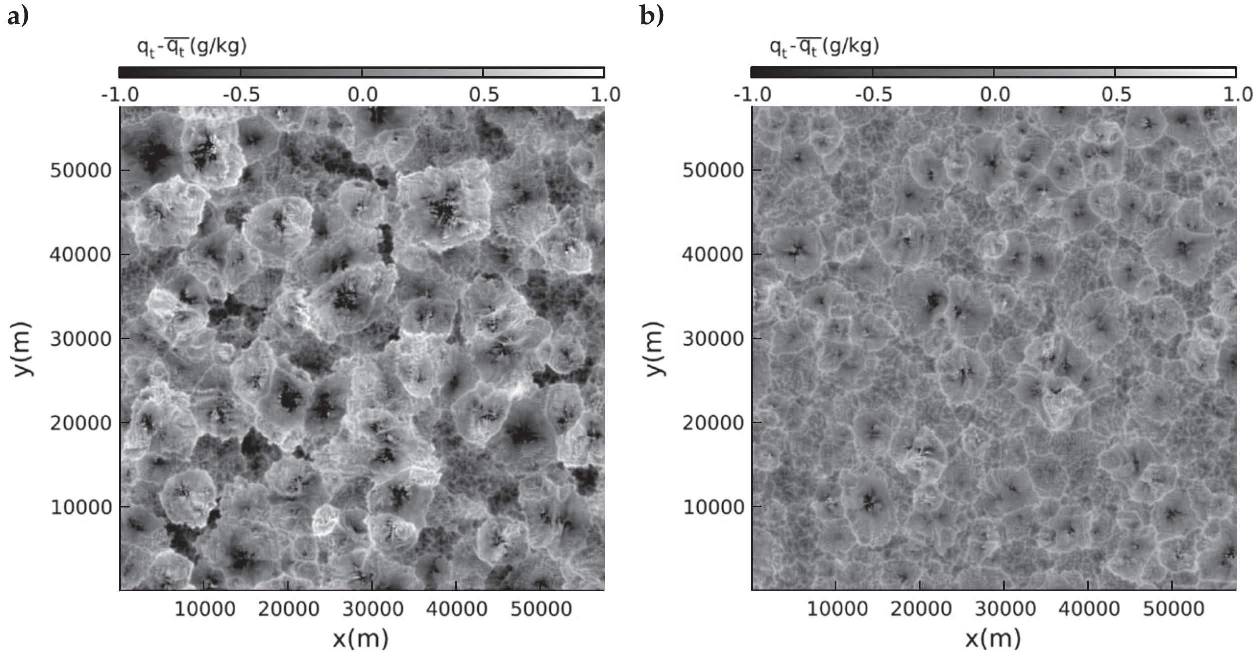

FIG. 8. Moisture deviation with respect to horizontal mean at 100 m after 420 min in (a) the reference simulation and (b) a modified simulation in which the subcloud variance of the thermodynamic variables (q_t and θ_l) was damped with $\tau = 600$ s.

the moisture perturbations with respect to the mean state at 100 m in Fig. 8. The centers of the cold pools are much dryer in the reference simulation because of the stronger downdrafts. Larger positive perturbations in the moisture field with respect to the mean state occur at the edges of the cold pools in the reference simulation. This is due to the cold pool centers being dryer in comparison with the edges as well as to the air at the gust front being in contact with the surface for a longer time. The discussion of the evolution of cold pools is limited in the present work, as we found similar results to Khairoutdinov and Randall (2006) in this respect. At the end of the simulation, only a few cold pools are left. The constant formation of new cold pools moistens and cools the boundary layer as a whole (Fig. 6), although the cold pools have relatively dry centers. Drying may become a dominant effect in simulations with more vigorous rainfall.

Note that the damping method in itself has only a direct effect on the signal amplitude, and not on the spectrum of the signal. However, there appears to be a strong indirect effect on the length scales. The small-scale fluctuations are created on a very short time scale by vertical mixing in the boundary layer, whereas large-scale fluctuations develop so slowly that damping effectively annihilates them. This result is consistent with earlier LES studies of transport of a decaying tracer in the boundary layer by Jonker et al. (2004). The thermodynamic variables do not merely play a passive role though: as the cold pools are driven by density currents, the amplitude of the buoyancy perturbation influences the horizontal spreading rate of the cold pools. This is a second way in which damping influences the length scales in the boundary layer [see, e.g., Parker (1996) for a simple model of the spreading cold pool].

In section 4, we will come back to the question whether local boundary layer extremes in thermodynamic properties play a role in the initiation of deep convection, or whether large-scale structures in the boundary layer are crucial.

b. *Cloud core mass flux and cloud size distribution*

To reconstruct how the modifications in the subcloud layer lead to a reduction of precipitation, we first look into the mass-flux profiles. We focus on the positively buoyant cloud core (points having $\theta_v - \overline{\theta_v} > 0$ and $q_l > 0$), rather than all cloudy points, because it appears that within a (volume-weighted) bulk-plume approach, such a decomposition more accurately captures the total water and liquid water potential temperature fluxes. The mass flux at cloud base is about equal between simulations (Fig. 9). In the upper troposphere the mass flux is much higher for the reference simulation. Clouds apparently reach deeper in this case.

What causes the absence of deeper clouds after modification? We consider the link between the cloud width and depth that was found by Grabowski et al. (2006). We identify individual clouds, as in Siebesma and Jonker (2001). The area of each of these three-dimensional clouds

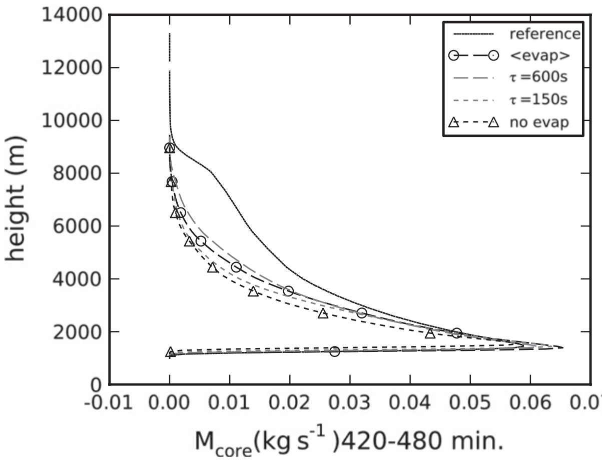

FIG. 9. Cloud core mass-flux profiles (eighth hour).

at each height (in the two-dimensional plane) is plotted in Fig. 10. This figure is a snapshot of all of the clouds at the end of the simulation for the reference case and the case where $\tau = 600$ s. Although clouds here are defined by the presence of liquid water, results for the cloud core are similar. Clouds are ordered by volume and their center is shifted along the x axis accordingly. They are plotted such that their width at each level in the figure is proportional to their effective width $2\sqrt{A(z)/\pi}$ on the same scale as the height axis [with $A(z)$ being the surface area of the cloud in the horizontal plane]. Comparison of the reference case with the modified case clearly shows that the widest clouds, which are also the deepest, do not appear in the ensemble of the modified case. This is compensated by a larger number of smaller clouds (with a volume between 10^8 and 10^9 m^3). This confirms the idea that the widest clouds in the ensemble make up the deep convection. In Fig. 7, it is shown that the widest clouds are also responsible for most of the surface rainfall.

c. Cloud properties

We subsequently investigate whether the conditionally sampled properties of the cloud core are different between simulations. When we consider the cloud core sampled excesses of q_t, θ_v, θ_l, and vertical velocity w in Fig. 11, the largest differences can be found in the θ_v and w profiles. All excesses are defined with respect to the mean state here since this is consistent with the approach of traditional plume models, but other approaches exist that distinguish the near and far environment (e.g., Jonker et al. 2008). The modest differences in vertical velocity may be due to the strongest updrafts in the reference simulation being accompanied by a larger number of cloud elements that are marginally buoyant and rise slowly at the edges of the larger clouds. The differences in mass flux at the higher level that we observed in Fig. 9 are mostly determined by differences in the cloud core area. The differences in q_t and θ_l between simulations are remarkably small. In the reference simulation, the cloud cores also feature higher θ_l in the upper troposphere, possibly due to stronger rain formation, which leads to parcels with lower q_t and higher θ_l. Cloud core volume-mean buoyancy excess remains limited to under 0.5 K in all simulations [as in Kuang and Bretherton (2006)], but the cloud cores maintain much larger buoyancy in the reference simulation as compared to the modified ones. We will look into differences in the in-cloud properties in more detail in the next section, where we consider the differences between shallow and deep clouds within the same cloud field.

d. Rainfall extremes

In Fig. 2, we already noticed that the mean surface rainfall rates are largely affected by reducing the subcloud variance of q_t and θ_l. The difference at 1200 m (above cloud base) shows that the decrease after modifying the

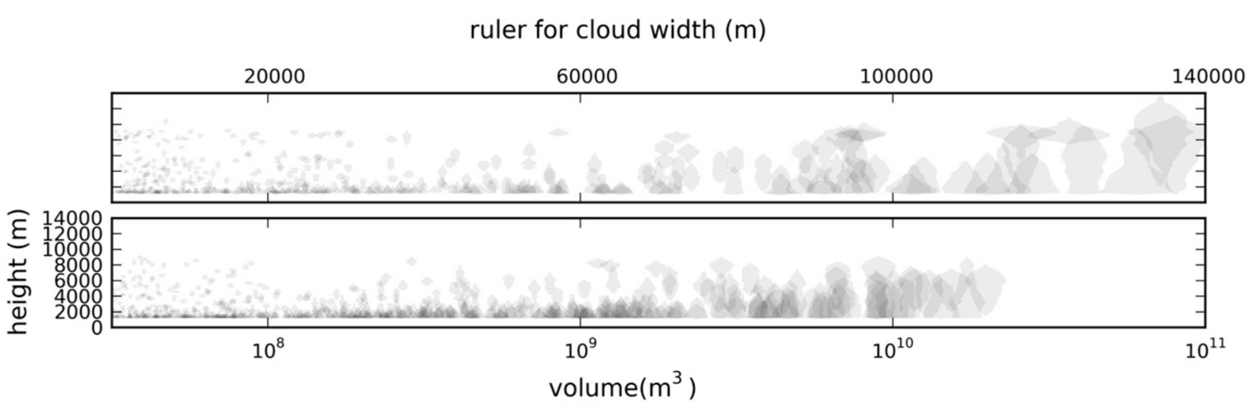

FIG. 10. Cloud ensemble at the end of the simulation for (top) the reference simulation and (bottom) a simulation with a damping time scale of 600 s. The top axis serves as a ruler for the effective cloud width on the same scale as cloud height. See text for details.

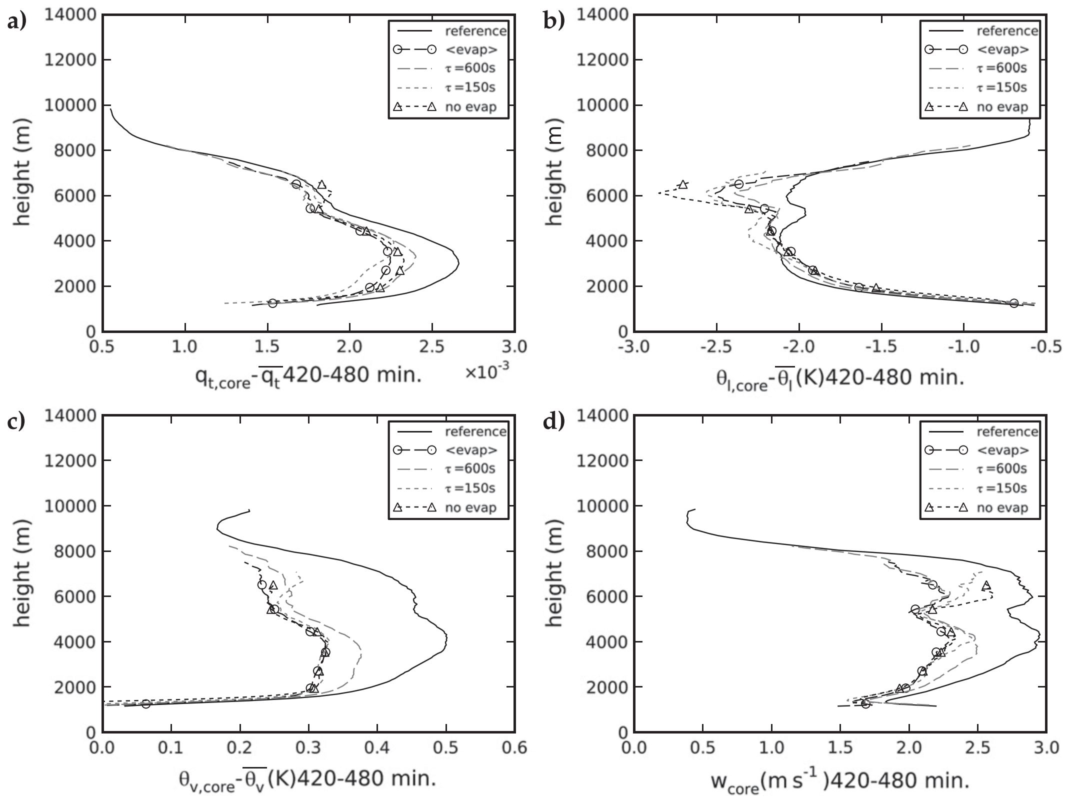

FIG. 11. Cloud-core excesses of (a) total specific humidity q_t, (b) liquid-water potential temperature θ_l, (c) buoyancy in θ_v units, and (d) vertical velocity in the cloud core (eighth hour).

subcloud layer feeds back on rain formation in the cloud layer itself. A plot of exceedance probabilities of rainfall rates at the surface (Fig. 12, after Lang et al. 2007) indicates that the decrease in the exceedance probability in the modified cases is largest for the strongest rainfall events. Whereas the probability of any rainfall (i.e., the fractional area where rainfall occurs, mentioned in the legend) is similar in the simulations with damping, the probability of rainfall in exceedance of 30 mm h^{-1} drops by a factor of 10 for the modified simulations. These larger rainfall rates were shown to correspond to the widest clouds in Fig. 7. In the simulation where no evaporation occurs, surface rainfall is found throughout the domain since there is no removal mechanism except for sedimentation, which is slow for small values of q_r.

4. What makes a deep cloud? Lagrangian studies

a. Lagrangian particle routine

Although the previous section shows the tight coupling between the subcloud layer and the cloud layer, one of the questions that remains open is the relative role of the local (thermo)dynamic properties of the parcels that enter the updrafts after cold pools form versus the importance of a change in large-scale structures in the subcloud layer.

To get a better idea of what aspects in the subcloud layer are really relevant with respect to the formation of deep clouds, investigation of Lagrangian particle trajectories may be useful. Lagrangian studies of deep convection have been performed before by Lin and Arakawa (1997), who focused on entrainment. The use of Lagrangian particles has the advantage that it allows us to study the behavior of the deepest clouds by sampling particles in the highest cloud tops and tracking some of these particles back to the subcloud layer. We can look at the properties of the corresponding air when it entered the cloud, and implicitly take into account ''distortions'' such as shear and cloud growth.

The particle routine has been used earlier in an investigation of mixing in shallow cumulus clouds by Heus et al. (2008). To minimize possible effects of excessive particle dispersion, the subgrid scheme for particle diffusion has been disabled in the current work.

b. Selection of deep convective trajectories

Initially, 1 000 000 particles are distributed randomly over the domain below 20 km. The local probability of a

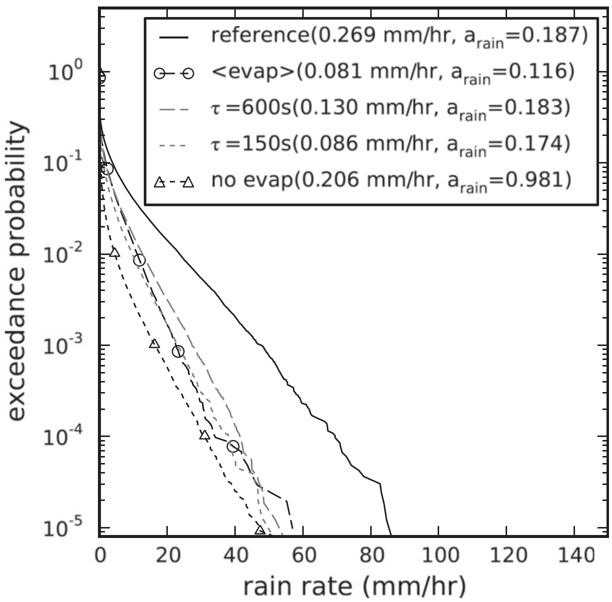

FIG. 12. Exceedance probabilities of surface rainfall rate during the last hour of the simulation, including a zero rainfall rate. The legend also displays the domain mean rainfall rate (mm h^{-1}) and the fractional area covered by rainfall a_{rain}.

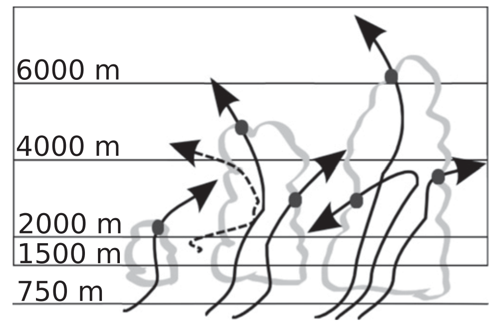

FIG. 13. Illustration of particle data postprocessing routine. Data of all trajectories exiting between two levels are combined. The dashed trajectory corresponds to a trajectory that does not originate from the subcloud layer and is left out of the statistics.

particle being initialized at a location is proportional to the density of air. Data on the particle trajectories are collected every 20 s. We will consider the particles that correspond to trajectories reaching from the subcloud layer up to a certain level in the cloud field (see Fig. 13). Four sets of trajectories were selected on the basis of the height at which they exit the cloud (the first time they are encountered in unsaturated air). The following ranges of exit heights are considered:

- 1500–2000 m
- 2000–4000 m
- 4000–6000 m
- >6000 m

Furthermore, all trajectories had to match the following criteria:

- The particle was below 1500 m when it entered the cloud (no lateral entrainment).
- The particle was below 750 m at some point in time during the 20 min before entering this cloud (i.e., the last time it was unsaturated).

Data of the trajectories between 10 min before cloud entry and the moment the particle exits the cloud were used in the analysis. The grid values in the LES are interpolated to the position of the particle. We consider deviations of q_t, θ_l, θ_v, and w from the mean horizontal state and the area of the cloud a particle is in. The data of the selected trajectories at each time step are binned by nearest 100-m level in the postprocessing. For the largest exit heights (>6000 m), we found the smallest dataset, which consisted of 2077 trajectories out of 1 million. To see if the results we obtained were reproducible, we repeated the experiment several times using different random deviations in the initial conditions.

c. Results

In this paper, we only discuss results corresponding to the reference case. The moist static energy ($h = c_pT + gz + L_vq_v$), q_t deviations with respect to the horizontal mean, and q_t tendencies due to microphysical processes (autoconversion/accretion rates) corresponding to trajectories with different exit heights are plotted in Fig. 14. The gray band indicates the spread between the upper and lower 10% of the trajectories exiting at more than 6000 m and thus shows the spread in individual particle properties in this exit height category.

The particles that exit at higher levels retain a slightly higher moist static energy, a variable that is to a good approximation conserved even in the presence of precipitation. However, the moist static energy is not constant with height for any of the sets of particles. Rather, it adjusts toward the mean profile for all sets of particles. This is in agreement with earlier studies by Khairoutdinov and Randall (2006), Romps and Kuang (2010a), and Del Genio and Wu (2010), who showed the absence of air with the same moist static energy as the air at the cloud base higher in the cloud layer. For q_t, the standard deviation of spatial variability over the whole domain and the volume-mean deviation of the buoyant cloud core are shown along with the deviations. In the cloud layer, the q_t excesses corresponding to the selected trajectories are similar to the cloud core excess.

For the total specific humidity, some of the differences between the trajectories can be attributed to differences in the rain formation rate, as shown in Fig. 14. The particles

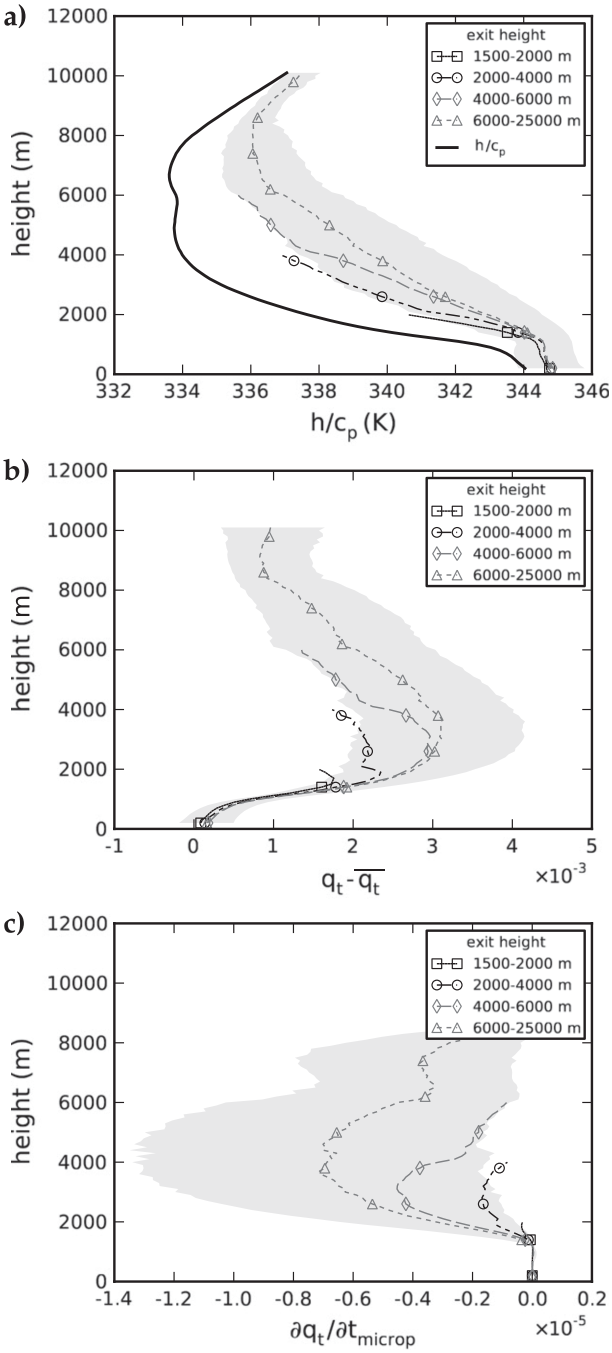

FIG. 14. Backtracked particle properties: (a) h/c_p, (b) q_t deviations with respect to the horizontal mean, and (c) tendencies in q_t due to microphysical processes (i.e., rain production rate due to autoconversion/accretion at the location of the particle, in the cloud layer. The gray band indicates the spread between the lower and upper 10% of properties from particles exiting above 6000 m.

that exit at a higher level correspond to larger rain formation rates. The differences in moist static energy can be regarded as a proxy for differences in plume entrainment rate. However, the signal of the moist static energy is more robust than that of the entrainment rate, as the moist static energy results from integrating the entrainment along the trajectory. We will come back to entrainment rates below.

Figure 15 zooms in on the subcloud layer particle properties. Here, deviations from the horizontal average at a given height of q_t, θ_v, and w are shown. The deviations look remarkably similar for the different exit height categories. Below cloud base, the particles were on average about 0.2 g kg^{-1} moister than their environment, a value that agrees well with the deviations that Tompkins (2001b) finds near the outflow boundary. The θ_v statistics show positively buoyant areas at the surface and in the cloud, but even the parcels that reach high into the troposphere have to "tunnel" through a barrier where they become negatively buoyant at cloud base. The w deviation of the particles is much more than the spatial standard deviation. It shows a slight decrease around cloud base, corresponding to the CIN layer we observed in θ_v.

Although all trajectory sets correspond to extreme subcloud updraft velocities and relatively moist parcels, the difference between trajectories with different exit levels is much smaller than the absolute perturbation. In q_t, a modest difference of about 0.1 g kg^{-1} can be identified (this difference was also found in runs with different initial perturbations). The corresponding latent heat is equivalent to a temperature difference of 0.25 K. The band corresponding to particles exiting at more than 6000 m also shows that there is no one-to-one correspondence between subcloud layer properties and the height a particle reaches. Romps and Kuang (2010b) used tracers to show that for shallow convection, the correlation between subcloud layer properties and cloud layer properties is also very poor (they found an even weaker signal).

The modest effects displayed by the Lagrangian particle analysis in the subcloud layer may seem paradoxical at first: it appears that the local (thermo)dynamic properties of the subcloud layer are poorly correlated to what happens in the cloud layer. On the other hand, the experiments of section 3 clearly show the variance of the thermodynamic variables in the subcloud layer was found to have a strong effect on the cloud layer.

Can we explain how the profiles of moist static energy evolve for the different exit height categories using an entraining plume model? Consider two entraining plumes in which a conserved scalar ϕ changes with height due to entrainment only:

$$\frac{\partial}{\partial z}\phi_1 = -\epsilon_1(\phi_1 - \phi_e),$$
$$\frac{\partial}{\partial z}\phi_2 = -\epsilon_2(\phi_2 - \phi_e). \qquad (4)$$

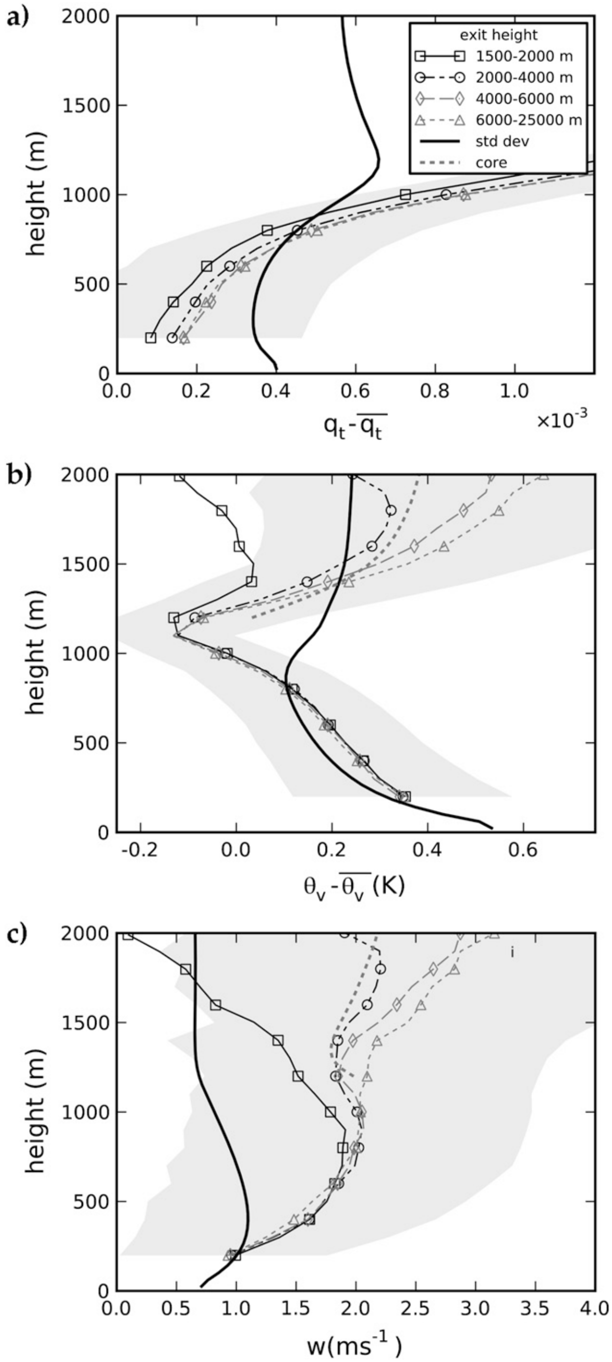

FIG. 15. Backtracked particle properties. Deviations with respect to the horizontal mean of (a) q_t, (b) θ_v, and (c) w in the subcloud layer.

We find that the difference in scalar properties evolves as

$$\frac{\partial}{\partial z}(\phi_1 - \phi_2) = -\epsilon_1(\phi_1 - \phi_e) + \epsilon_2(\phi_2 - \phi_e). \quad (5)$$

This implies that when a fixed entrainment rate $\epsilon_1 = \epsilon_2$ is taken for both parcels, the difference in ϕ will decrease with height, which is contrary to our findings for moist static energy. However, if the parcels experience a different entrainment rate, the difference in their properties can increase. If we consider the case where $\phi_1 > \phi_2 > \phi_e$, this will happen if

$$\epsilon_1 < \epsilon_2 \frac{(\phi_2 - \phi_e)}{(\phi_1 - \phi_e)}. \quad (6)$$

Figure 16 shows the backtracked entrainment rate of each set of particles (using the mean moist static energy of each set). The exit height categories indeed show different plume entrainment rates for moist static energy. This is even the case if we consider only the two sets with exit heights above 4000 m and look just above cloud base (the strong increase in entrainment at higher levels for each exit height category is partly due to particles that are no longer positively buoyant). Some plume models can account for a positive feedback between a stronger thermodynamic excess and a reduced entrainment rate, for example by making the entrainment rate depend on vertical velocity (which in itself depends on buoyancy; e.g., Neggers et al. 2002).

We investigate whether the entrainment rate could be related to cloud size, as suggested by Grabowski et al. (2006). To explore this idea, we combine the Lagrangian trajectories with Eulerian information on the structures in the cloud and subcloud layer. First, we observe that the particles reaching higher levels are already embedded in wider clouds at cloud base (Fig. 17). The differences in cloud radius between the particle sets with different exit heights are of the same order as the variation within one set (unlike the difference between subcloud thermodynamic variables, where differences between sets are much smaller). This implies that, above cloud base, the wider clouds are on average better at retaining their thermodynamic excesses. Given the results from the previous section, we wonder if we can relate the wider clouds to the subcloud layer. This inspired us to look again into the spatial distribution of the dynamic and thermodynamic variables, but combined with the Lagrangian data. We will consider mostly cross sections in the upper boundary layer, as we expect these to correlate better with cloud base.

The spatial distribution of the vertical velocity and specific humidity excess at 840 m together with those particles that enter the cloud within 20 min are plotted in Fig. 18. The particles are marked by exit height. A random subset of the particles exiting at less than 2000 m is displayed, with an equal number of particles as the set that exits above 6000 m. The zones where multiple

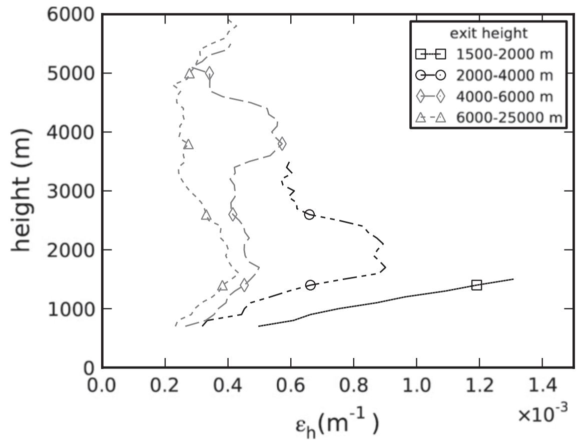

FIG. 16. Backtracked particle properties. Effective plume entrainment rate for moist static energy corresponding to the different exit height categories.

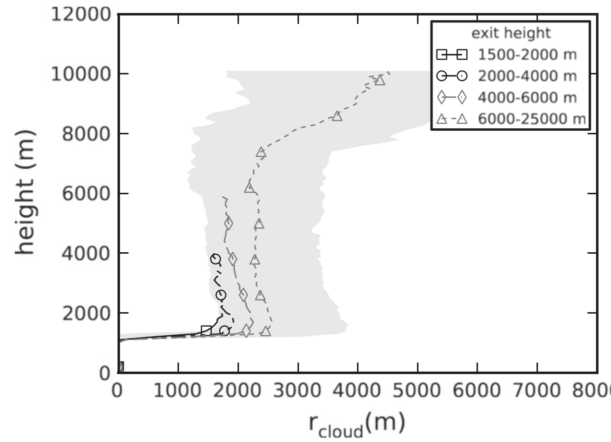

FIG. 17. Backtracked particle properties: cloud radius.

outflow boundaries intersect appear to be favorable for the formation of new deep convection [in agreement with Tompkins (2001b)], whereas shallow convection can be found at other places as well. The size of the updraft clusters in the boundary layer is much smaller than the size of the cold pools. This disparity in length scales was also found in the convective boundary layer (Jonker et al. 1999) and in other simulations of deep convection (Moeng et al. 2009). We also find that although moisture extrema coincide with the location of the edges of cold pools, the correspondence between the vertical velocity signal and the location of particles that are about to enter the cloud is much better (we have also considered potential temperature excesses and moisture excesses at a lower level, but vertical velocity appeared the best indicator). This is in agreement with the observation that the vertical velocity perturbation of the particles that enter the cloud is much larger than the standard deviation of vertical velocity, whereas the moisture perturbations of the particles are smaller the standard deviation (Fig. 15).

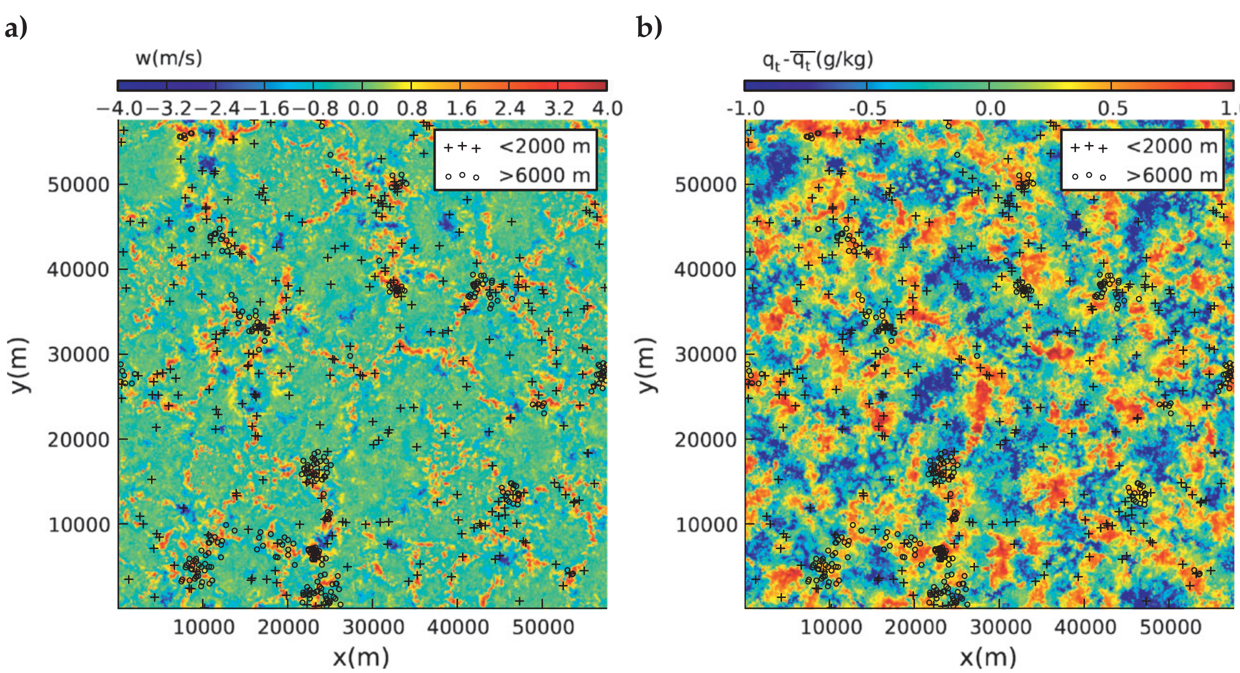

FIG. 18. (a) Vertical velocity and (b) moisture anomalies with respect to the horizontal mean at 840 m after 420 min. The markers indicate random subsets of subcloud layer particle positions for particles that will enter a cloud within 20 min. The marker symbols indicate different corresponding exit heights.

The spatial location of particles in the subcloud layer holds some clues regarding the role of the subcloud layer. In the next section, we will propose two pathways for further studies of the role of subcloud layer that are based on this result.

5. Summary and discussion

Through a series of sensitivity experiments, we look into a feedback loop that rapidly accelerates the formation of deep convective clouds after the onset of precipitation. In runs where cold pool formation is suppressed, the widest and deepest clouds, which correspond to the heaviest rain rates, are absent. This feedback loop, which was identified in earlier work of Grabowski et al. (2006) and Khairoutdinov and Randall (2006), is shown to depend on the presence of cold pools rather than differences in the vertical profiles of the mean state of the subcloud layer. The feedback loop plays a role in the rapid transition from shallow cumulus convection to heavily precipitating convection over land and is important for the timing of precipitation in the diurnal cycle.

Using Lagrangian particle analysis, we investigate whether the differences between trajectories corresponding to shallow and deep clouds can be traced back to subcloud layer properties. There is a small difference in the mean specific humidity of the different sets of particles, but a much wider spread in the individual particle properties occurs within each set.

The distributions of thermodynamic properties are relatively narrow at cloud base, and these distributions widen in the cloud layer, which confirms the study of Kuang and Bretherton (2006). Our findings are also in agreement with those of Romps and Kuang (2010b), who found that in shallow convection, subcloud layer properties are poorly correlated to parcel dilution in the cloud layer. Romps and Kuang interpreted the effect of mixing in terms of stochastic entrainment. We argue, however, that the organization of the subcloud layer plays an important role.

In contrast to the poor correlation between exit height and the local properties of the particles in the subcloud layer, we find a strong correlation between exit height and cloud size at cloud base. This strong correlation points to a limitation of models that describe the evolution of an updraft in terms of the properties of the mean environment and the local updraft properties at cloud base only. The notion that the cloud size at cloud base is crucial for cloud depth, but that this dependence is hardly manifested in the mean cloud-base thermodynamic properties confirms earlier studies of this relation in shallow cumulus by Dawe and Austin (2011). The current work shows that this is also the case in deeper convection. Our simulations with a modified subcloud layer and the specific location of particles that form deep clouds in the subcloud layer (Fig. 18) suggest an active role for the subcloud layer. We put forward two ideas that may partly explain the role of the subcloud layer and would merit future work:

- The near environment hypothesis: Clouds tend to form along the gust fronts (see also Fig. 7), but the deepest clouds form at their intersection. This could be due to the fact that such clouds are surrounded by other clouds on all sides and will interact less with "hostile" noncloudy air, allowing them to provide for wider cloud bases. The particle trajectory method does not pick up the organization when the properties are concerned because it does not account for the neighboring environment. However, when the particles are related to spatial information, such as cloud size and the spatial distribution of the vertical velocity, the signal can be recovered.
- The time scale hypothesis: The formation of deep clouds takes place over a much longer time scale than the time scale of individual parcel uplift. It is not so much the different nature of the parcels that determines whether a deep or a shallow cloud starts to form, but rather the fact that there is a more persistent updraft for deeper clouds. Furthermore, once a deeper cloud exists, it will also cause stronger surface convergence than a shallow cloud, leading to an inflow of air with less extreme properties associated with parcels coming from a position farther away from the point where the cloud is initiated. This helps to mask differences in thermodynamic properties between shallow and deep clouds. It may be useful to study the life cycle of the deeper clouds in order to see if this effect plays a role.

These ideas differ from the mechanism for initiation of deep clouds proposed by Tompkins (2001b), who investigated a case over sea. Tompkins also noticed triggering of deep convection at the outflow boundary and argued that the rate at which fluxes recover temperature and moisture perturbations plays a major role. Here, we are limited to a case with constant surface fluxes. However, we find that in our case the large-scale structures in the vertical velocity field give a better indication of the preferential location where deep clouds form than those in the thermodynamic fields, although both show extremes at the edges of cold pools.

The difference in conclusions may be due to the method that was used in the data analysis. Tompkins determines the statistics as a function of the distance to the center of the nearest cold pool. The sharp edges of positive vertical velocity that occur at the outflow boundary are not very pronounced in these statistics. By backtracking the particles in deep convection, we can recover their relation to the vertical velocity field in more detail.

The current work emphasizes that a coupled model of the subcloud and cloud layer is needed to obtain a good representation of deep convection. Such a model can either be highly idealized in the form of a model of convection with memory (e.g., Mapes and Neale 2011) or can be rooted in a physical model of the cold pool circulation (e.g., Grandpeix and Lafore 2010).

Acknowledgments. This work was sponsored by the National Computing Facilities foundation (NCF) for the use of supercomputer facilities, with financial support of NWO. The authors wish to thank Dr. Chien-Ming Wu for his help in constructing the initial profiles for this case and three reviewers for their constructive comments.

APPENDIX

Single-Moment Microphysics Scheme

The scheme of Grabowski (1998) serves as the basis for the one-moment microphysics scheme used in this study. As in Grabowski (1998), the saturation mixing ratio is calculated as a linear combination of the saturation mixing over cloud ice and the saturation mixing ratio over cloud water, where the partitioning depends on temperature:

$$q_{\mathrm{sat}}(T,p) = \omega(T)q_{\mathrm{sat},l}(T,p) + [1 - \omega(T)]q_{\mathrm{sat},i}(T,p). \tag{A1}$$

Here, ω is the relative weight given to saturation with respect to the liquid and ice phase. Saturation pressure with respect to cloud water and cloud ice has been tabulated using the equations given in Murphy and Koop (2005). Rather than using the mean particle size in some parts of the microphysics scheme, all tendencies were obtained by integration over the full droplet spectrum (cf. Tomita 2008). This mitigates the overestimation of rain evaporation that a one-moment scheme has in comparison to double-moment schemes. Also like Tomita (2008), we have taken into account the dependence of terminal velocity on air density. As in Khairoutdinov and Randall (2003), an additional graupel class was used for precipitation. Mass–diameter and terminal velocity parameters for graupel have been taken from the work of Tomita (2008). The diagnostic partitioning of solid precipitation into snow and graupel is made on the basis of temperature, following the partitioning given in Khairoutdinov and Randall (2003).

REFERENCES

Bechtold, P., J.-P. Chaboureau, A. Beljaars, A. K. Betts, M. Köhler, M. Miller, and J.-L. Redelsperger, 2006: The simulation of the diurnal cycle of convective precipitation over land in a global model. *Quart. J. Roy. Meteor. Soc.,* **130,** 3119–3137.

Betts, A. K., and C. Jakob, 2002: Evaluation of the diurnal cycle of precipitation, surface thermodynamics, and surface fluxes in the ECMWF model using LBA data. *J. Geophys. Res.,* **107,** 8045, doi:10.1029/2001JD000427.

Bryan, G. H., and J. M. Fritsch, 2004: A reevaluation of ice–liquid water potential temperature. *Mon. Wea. Rev.,* **132,** 2421–2431.

——, J. C. Wyngaard, and J. M. Fritsch, 2003: Resolution requirements for the simulation of deep moist convection. *Mon. Wea. Rev.,* **131,** 2394–2416.

Carbone, R. E., J. W. Wilson, T. D. Keenan, and J. M. Hacker, 2000: Tropical island convection in the absence of significant topography. Part I: Life cycle of diurnally forced convection. *Mon. Wea. Rev.,* **128,** 3459–3480.

Dawe, J. T., and P. H. Austin, 2011: Statistical analysis of a LES shallow cumulus cloud ensemble using a cloud tracking algorithm. *Atmos. Chem. Phys. Discuss.,* **11,** 23 231–23 273, doi:10.5194/acpd-11-23231-2011.

Del Genio, A. D., and J. Wu, 2010: The role of entrainment in the diurnal cycle of continental convection. *J. Climate,* **23,** 2722–2738, doi:10.1175/2009JCLI3340.1.

Derbyshire, S. H., I. Beau, P. Bechtold, J.-Y. Grandpeix, J.-M. Piriou, J.-L. Redelsperger, and P. M. M. Soares, 2006: Sensitivity of moist convection to environmental humidity. *Quart. J. Roy. Meteor. Soc.,* **130,** 3055–3079.

Grabowski, W. W., 1998: Toward cloud resolving modeling of large-scale tropical circulations: A simple cloud microphysics parameterization. *J. Atmos. Sci.,* **55,** 3283–3298.

——, and Coauthors, 2006: Daytime convective development over land: A model intercomparison based on LBA observations. *Quart. J. Roy. Meteor. Soc.,* **132,** 317–344, doi:10.1256/qj.04.147.

Grandpeix, J.-Y., and J.-P. Lafore, 2010: A density current parameterization coupled with Emanuel's convection scheme. Part I: The models. *J. Atmos. Sci.,* **67,** 881–897.

Guichard, F., and Coauthors, 2004: Modelling the diurnal cycle of deep precipitating convection over land with cloud-resolving models and single-column models. *Quart. J. Roy. Meteor. Soc.,* **130,** 3139–3172, doi:10.1256/qj.03.145.

Heus, T., G. van Dijk, H. J. J. Jonker, and H. E. A. Van den Akker, 2008: Mixing in shallow cumulus clouds studied by Lagrangian particle tracking. *J. Atmos. Sci.,* **65,** 2581–2597.

——, and Coauthors, 2010: Formulation of and numerical studies with the Dutch Atmospheric Large-Eddy Simulation (DALES). *Geosci. Model. Dev. Discuss.,* **3,** 99–180.

Holloway, C. E., and J. D. Neelin, 2009: Moisture vertical structure, column water vapor, and tropical deep convection. *J. Atmos. Sci.,* **66,** 1665–1683.

Jonker, H. J. J., P. G. Duynkerke, and J. W. M. Cuijpers, 1999: Mesoscale fluctuations in scalars generated by boundary layer convection. *J. Atmos. Sci.,* **56,** 801–808.

——, J. Vilà-Guerau de Arellano, and P. G. Duynkerke, 2004: Characteristic length scales of reactive species in a convective boundary layer. *J. Atmos. Sci.,* **61,** 41–56.

——, T. Heus, and P. P. Sullivan, 2008: A refined view of vertical mass transport by cumulus convection. *Geophys. Res. Lett.,* **35,** L07810, doi:10.1029/2007GL032606.

Khairoutdinov, M. F., and D. A. Randall, 2003: Cloud resolving modeling of the ARM summer 1997 IOP: Model formulation, results, uncertainties, and sensitivities. *J. Atmos. Sci.,* **60,** 607–625.

——, and ——, 2006: High-resolution simulation of shallow-to-deep convection transition over land. *J. Atmos. Sci.,* **63,** 3421–3436.

Kingsmill, D. E., 1995: Convection initiation associated with a sea-breeze front, a gust front, and their collision. *Mon. Wea. Rev.,* **123,** 2913–2933.

Krueger, S. K., 1988: Numerical simulation of tropical cumulus clouds and their interaction with the subcloud layer. *J. Atmos. Sci.,* **45,** 2221–2250.

Kuang, Z., and C. S. Bretherton, 2006: Mass-flux scheme view of a high-resolution simulation of a transition from shallow to deep cumulus convection. *J. Atmos. Sci.,* **63,** 1895–1909.

Lang, S., W. K. Tao, J. Simpson, R. Cifelli, S. Rutledge, W. Olson, and J. Halverson, 2007: Improving simulations of convective systems from TRMM LBA: Easterly and westerly regimes. *J. Atmos. Sci.,* **64,** 1141–1164.

Lima, M. A., and J. W. Wilson, 2008: Convective storm initiation in a moist tropical environment. *Mon. Wea. Rev.,* **136,** 1847–1864.

Lin, C., and A. Arakawa, 1997: The macroscopic entrainment processes of simulated cumulus ensemble. Part I: Entrainment sources. *J. Atmos. Sci.,* **54,** 1027–1043.

Mapes, B., and R. Neale, 2011: Parameterizing convective organization to escape the entrainment dilemma. *J. Adv. Model. Earth. Sys.,* **3,** M06004, doi:10.1029/2011MS000042.

Martins, J. P. A., 2011: Cumulus boundary layers in the atmosphere: High resolution models and satellite observations. Ph.D. thesis, Universidade de Lisboa, 95 pp. [Available online at http://repositorio.ul.pt/bitstream/10451/4835/1/ulsd061699_td_Joao_Martins.pdf.]

Moeng, C.-H., M. A. LeMone, M. F. Khairoutdinov, S. K. Krueger, P. A. Bogenschutz, and D. A. Randall, 2009: The tropical marine boundary layer under a deep convection system: A large-eddy simulation study. *J. Adv. Model. Earth. Sys.,* **1** (16), doi:10.3894/JAMES.2009.1.16.

Moncrieff, M. W., and C. Liu, 1999: Convection initiation by density currents: Role of convergence, shear, and dynamical organization. *Mon. Wea. Rev.,* **127,** 2455–2464.

Murphy, D. M., and T. Koop, 2005: Review of the vapour pressures of ice and supercooled water for atmospheric applications. *Quart. J. Roy. Meteor. Soc.,* **131,** 1539–1565.

Neggers, R. A. J., A. P. Siebesma, and H. J. J. Jonker, 2002: A multiparcel model for shallow cumulus convection. *J. Atmos. Sci.,* **59,** 1655–1668.

Parker, D. J., 1996: Cold pools in shear. *Quart. J. Roy. Meteor. Soc.,* **122,** 1655–1674, doi:10.1256/smsqj.53508.

Petch, J. C., P. N. Blossey, and C. S. Bretherton, 2008: Differences in the lower troposphere in two- and three-dimensional cloud-resolving model simulations of deep convection. *Quart. J. Roy. Meteor. Soc.,* **134,** 1941–1946.

Rauber, R. M., and Coauthors, 2007: Rain in Shallow Cumulus over the Ocean: The RICO campaign. *Bull. Amer. Meteor. Soc.,* **88,** 1912–1928.

Rio, C., F. Hourdin, J. Grandpeix, and J. Lafore, 2009: Shifting the diurnal cycle of parameterized deep convection over land. *Geophys. Res. Lett.,* **36,** L07809, doi:10.1029/2008GL036779.

Robe, F. R., and K. A. Emanuel, 2001: The effect of vertical wind shear on radiative–convective equilibrium states. *J. Atmos. Sci.,* **58,** 1427–1445.

Romps, D. M., and Z. Kuang, 2010a: Do undiluted convective plumes exist in the upper tropical troposphere? *J. Atmos. Sci.,* **67,** 468–484.

——, and ——, 2010b: Nature versus nurture in shallow convection. *J. Atmos. Sci.,* **67,** 1655–1666.

Rotunno, R., J. B. Klemp, and M. L. Weisman, 1988: A theory for strong, long-lived squall lines. *J. Atmos. Sci.,* **45,** 463–485.

Siebesma, A. P., and H. J. J. Jonker, 2001: Anomalous scaling of cumulus cloud boundaries. *Phys. Rev. Lett.,* **85,** 214–217.

Silva Dias, M. A. F., and Coauthors, 2002: Cloud and rain processes in a biosphere–atmosphere interaction context in the Amazon region. *J. Geophys. Res.,* **107,** 8072, doi:10.1029/2001JD000335.

Smolarkiewicz, P. K., L. G. Margolin, and A. A. Wyszogrodzki, 2001: A class of nonhydrostatic global models. *J. Atmos. Sci.,* **58,** 349–364.

Stirling, A. J., and J. C. Petch, 2004: The impacts of spatial variability on the development of convection. *Quart. J. Roy. Meteor. Soc.,* **130,** 3189–3206.

Tomita, H., 2008: New microphysical schemes with five and six categories by diagnostic generation of cloud ice. *J. Meteor. Soc. Japan,* **86A,** 121–142.

Tompkins, A. M., 2001a: Organization of tropical convection in low vertical wind shears: The role of water vapor. *J. Atmos. Sci.,* **58,** 529–545.

——, 2001b: Organization of tropical convection in low vertical wind shears: The role of cold pools. *J. Atmos. Sci.,* **58,** 1650–1672.

Waite, M. L., and B. Khouider, 2010: The deepening of tropical convection by congestus preconditioning. *J. Atmos. Sci.,* **67,** 2601–2615.

Weckwerth, T. M., and R. M. Wakimoto, 1992: The initiation and organization of convective cells atop a cold-air outflow boundary. *Mon. Wea. Rev.,* **120,** 2169–2187.

Wilson, J. W., and D. L. Megenhardt, 1997: Thunderstorm initiation, organization, and lifetime associated with Florida boundary layer convergence lines. *Mon. Wea. Rev.,* **125,** 1507–1525.

Wu, C. M., B. Stevens, and A. Arakawa, 2009: What controls the transition from shallow to deep convection? *J. Atmos. Sci.,* **66,** 1793–1806.

Xie, S., T. Hume, C. Jakob, S. A. Klein, R. B. McCoy, and M. Zhang, 2010: Observed large-scale structures and diabatic heating and drying profiles during TWP-ICE. *J. Climate,* **23,** 57–79.

Zhang, Y., and S. Klein, 2010: Mechanisms affecting the transition from shallow to deep convection over land: Inferences from observations of the diurnal cycle collected at the ARM Southern Great Plains site. *J. Atmos. Sci.,* **67,** 2943–2959.

Zuidema, P., and Coauthors, 2012: On trade-wind cumulus cold pools. *J. Atmos. Sci.,* **69,** 258–280.